Critical porosity of melt segregation during crustal melting: Constraints from zonation of peritectic garnets in a dacite volcano

Xun Yu [a,b,*], Cin-Ty A. Lee [a]

[a] Department of Earth Sciences, Rice University, Houston, TX 77005, USA
[b] State Key Laboratory for Mineral Deposits Research, School of Earth Sciences and Engineering, Nanjing University, Nanjing 210023, China

ABSTRACT

The presence of leucogranitic dikes in orogenic belts suggests that partial melting may be an important process in the lower crust of active orogenies. Low seismic velocity and low electrical resistivity zones have been observed in the lower crust of active mountain belts and have been argued to reflect the presence of partial melt in the deep crust, but volcanoes are rare or absent above many of these inferred melt zones. Understanding whether these low velocity zones are melt-bearing, and if so, why they do not commonly erupt, is essential for understanding the thermal and rheologic structure of the crust and its dynamic evolution. Central to this problem is an understanding of how much melt can be stored before it can escape from the crust via compaction and eventually erupt. Experimental and theoretical studies predict trapped melt fractions anywhere from <5% to >30%. Here, we examine Mn growth-zoning in peritectic garnets in a Miocene dacite volcano from the ongoing Betic–Rif orogeny in southern Spain to estimate the melt fraction at the time of large-scale melt extraction that subsequently led to eruption. We show that the melt fraction at segregation, corresponding approximately to the critical melt porosity, was ~30%, implying significant amounts of melt can be stored in the lower crust without draining or erupting. However, seismic velocities in the lower crust beneath active orogenic belts (southern Spain and Tibet) as well as beneath active magmatic zones (e.g., Yellowstone hotspot) correspond to average melt porosities of <10%, suggesting that melt porosities approaching critical values are short-lived or that high melt porosity regions are localized into heterogeneously distributed sills or dikes, which individually cannot be resolved by seismic studies.

© 2016 Elsevier B.V. All rights reserved.

1. Introduction

Crustal melting is thought to be an important process in controlling the chemical and structural evolution of orogenic belts. For example, highly incompatible elements, such as heat-producing elements like U, Th and K, are preferentially partitioned into melts, which rise to the surface and concentrate these elements in the upper crust. Melts can also rheologically weaken rocks, facilitating ductile deformation in the lower crust (Beaumont et al., 2001; Hodges, 2006). Understanding when and how crustal melts segregate from their partially molten source regions is thus important. One key quantity is the critical melt fraction (mass fraction of melt) or melt-filled porosity (volume fraction) at which melts segregate from a partially molten rock (Arzi, 1978; Renner et al., 2000; Rosenberg and Handy, 2005; Van der Molen and Paterson, 1979; Wickham, 1987). This critical porosity is controlled by the com-

petition between the driving force of melt segregation (melt buoyancy and deviatoric stresses) and viscous resisting forces associated with the transport of the melt through the permeable rock as well as the deformability of the partially molten rock itself (McKenzie, 1984). Permeability depends on melt viscosity, porosity and interconnectivity of the solid matrix. The lower the critical melt porosity, the more efficient melt segregation is, but the less melt that can be retained in the residuum, minimizing the effects of rock weakening. In the mantle, where melts are basaltic and of low viscosity and the solid matrix is hot and weak, critical melt porosities are thought to be significantly less than 1% (e.g., Sims et al., 1999). In contrast, crustal melts are silicic and cooler and thus are several orders of magnitude more viscous than basalts, so higher critical melt porosities in the crust are expected (e.g., Rosenberg and Handy, 2005; Rutter and Neumann, 1995).

Exactly what the critical melt porosity is for felsic systems is debated. Theoretical considerations and deformation experiments yield critical porosities for granitic melts ranging from 20 to 50% (Arzi, 1978; Renner et al., 2000; Rosenberg and Handy, 2005; Van der Molen and Paterson, 1979; Wickham, 1987). However, it
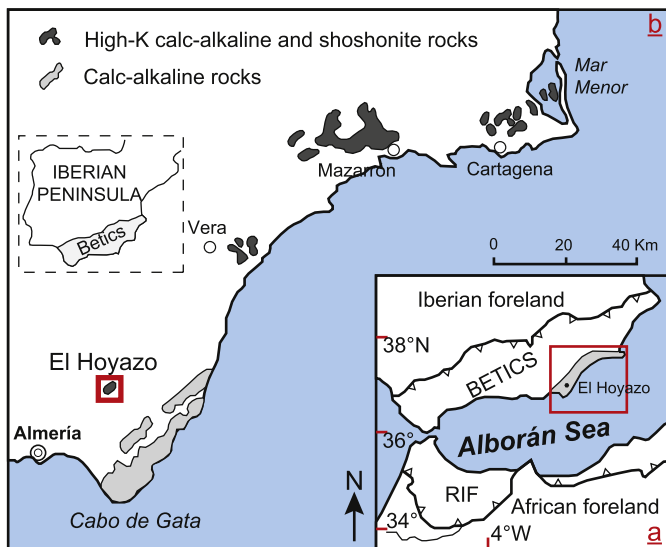
Fig. 1. The Neogene Volcanic Province of the southeastern Betic Orogeny in Spain, showing the location of Cerro del Hoyazo and other Miocene volcanics. Inset shows the volcanic province in the context of the Alboran sea domain and Spain. Figure is modified from Cesare and Gomez-Pugnaire (2001).

has also been shown that the volume increase associated with melting can result in over-pressures that cause brittle failure, allowing melts to escape at porosities lower than 10% (e.g., Rushmer, 1995, 2001), but to what extent such a process can lead to large-scale melt segregation is unclear.

Evaluating these scenarios in nature generally requires geochemical mass balance approaches or textural observations. Leucosomes and melanosomes in migmatites are consistent with cm-scale segregation at melt fractions larger than 20% (e.g., Berger and Kalt, 1999), but whether the presence of leucosomes is applicable to melt transport on km lengthscales is unclear. Geochemical mass balance considerations have also been applied to felsic plutons and lavas. For example, the elemental compositions of leucogranitic plutons and dikes in southern Tibet are suggestive of low melt mass fractions relative to the unmelted protolith (<10 wt.%) (e.g., Harris et al., 1995), but the meaning of estimated melt fractions is unclear because melt fractions determined by mass balance represent the integrated melts, formed by pooling and mixing of segregated melts (e.g., Sawyer, 1996), and do not necessarily correspond to the melt porosity at the time of segregation.

Here, we present a more direct way of constraining the melt porosity at segregation by examining elemental zoning in peritectic garnets from Cerro del Hoyazo, a 6.3 Ma dacite volcano in the Neogene volcanic province of southeastern Spain (Fig. 1). Volcanism here is a product of recent thinning or removal of the lithospheric mantle beneath the Betic Cordilleran orogen (Platt et al., 2013; Turner et al., 1999; Vissers et al., 1995). Cerro del Hoyazo is an almandine-bearing biotite–cordierite–labradorite dacite consisting of 10–15 vol.% xenoliths of partially melted restites (e.g., almandine–biotite–sillimanite gneiss and quartz–cordierite gneiss) (Acosta-Vigil et al., 2007, 2010; Álvarez-Valero et al., 2005; Cesare and Gomez-Pugnaire, 2001; Cesare et al., 1997; Zeck, 1970; Zeck and Williams, 2002). The dacites and restite xenoliths have been shown to be complementary via partial melting of a metapelite at intermediate pressures (5–7 kbar) (e.g., Acosta-Vigil et al., 2010; Cesare et al., 1997; Perini et al., 2009). Peritectic garnets, which formed by biotite-dehydration melting (Le Breton and Thompson, 1988; Vielzeuf and Holloway, 1988), are common in both the dacitic lavas and restite xenoliths. The changing composition of the melt during progressive melting is recorded by the garnet as it grows, such that the composition of the garnet rim reflects the

composition of the melt at the time garnets were entrained into the melt, providing a minimum estimate of the porosity at the time of melt segregation.

2. Methods

We examined five euhedral garnet grains (2 to 4.5 mm in diameter) without inclusions (Figs. 2 and 3). Major and trace elemental compositional transects were measured by laser ablation inductively coupled plasma mass spectrometry (LA-ICP-MS) with a ThermoFinnigan Element 2 equipped with a New Wave 213 nm laser ablation system at Rice University. External standards used for LA-ICP-MS analysis were United States Geological Survey basaltic glasses (BHVO2g, BCR2g, and BIR1g) using standard values from Gao et al. (2002). Laser ablation was conducted with a fluence of 18 J/cm^2, 10 Hz frequency, and 55 μm spot size. Prior to measurement, the instrument was tuned by controlling the sample gas (Ar) to achieve a sensitivity of 250,000 cps on 15 ppm La in BHVO2g in low mass resolution ($m/\Delta m \sim 300$). Major element and high field strength element are measured in medium mass resolution, while rare earth elements were measured in low mass resolution. Raw data were converted to concentrations using an in-house data reduction program (http://www.cintylee.org/s/Laser-RAWDATA-TEMPLATE.xls) that removed background signal intensities and elemental fractionation with external standards. Signal intensities were normalized to an internal standard (^{43}Ca), and time-resolved intervals were integrated. All measured data are showed in Tables S1 and S2.

To complement the elemental transects, elemental mapping of garnets was determined using a Horiba XGT-7200 X-ray analytical microscope at Rice University. This instrument is equipped with an X-ray guide tube of either 50 μm or 400 μm diameter with an Rh target. The instrument emits a high-energy micro X-ray beam up to 50 kV and 1 mA. Elements from Na to U can be detected by an energy-dispersive Si drift detector. Elemental mapping was done for major elements under full vacuum condition, with an acceleration voltage of 50 kV, 50 μm capillary, 200–400 s survey time per-frame, and 4 accumulations (see Jiang et al., 2015). The mapping results are shown in Figs. 2A and S1.

3. Results

The garnets are primarily almandine ($>80\%$) in composition, but all are systematically zoned. The compositions are identical to the garnets (Fig. 2B) previously studied from the same volcano and interpreted to have a peritectic origin based on peraluminous melt inclusions within the garnet (Álvarez-Valero et al., 2005, 2007; Cesare et al., 2005). Garnets increase in Fe and decrease in Mg and Mn towards the rim (Figs. 3 and S2). Heavy rare earth elements (HREEs) and Y also decrease monotonically towards the rim (Figs. 4A, 4B and S2). In particular, the HREEs, Y and Mn show bell-shaped, or concave downward, rim-to-rim profiles. Normalized REE abundance patterns show strong depletion in light rare earths (LREEs) but enrichments in HREEs, which is typical of garnets. However, REE abundance patterns develop humped appearances towards the rim as a result of preferential depletion of HREEs from the rock-magma matrix with progressive garnet growth (Fig. 4A, B). Core Mn and HREE concentrations are variable, but all garnets share the same rim trace element composition, indicating that all garnets record the same final equilibration conditions despite nucleating and growing at different times. Also of interest are Zr zonation profiles, which show a slight increase from core to rim, followed by a decrease in the outermost rim (Fig. 3). Sr and Eu, two elements which are considered incompatible in garnets, are enriched in the cores of some garnets, but exhibit an abrupt 100-fold decrease towards the rim (Fig. 4C, D, E, F).
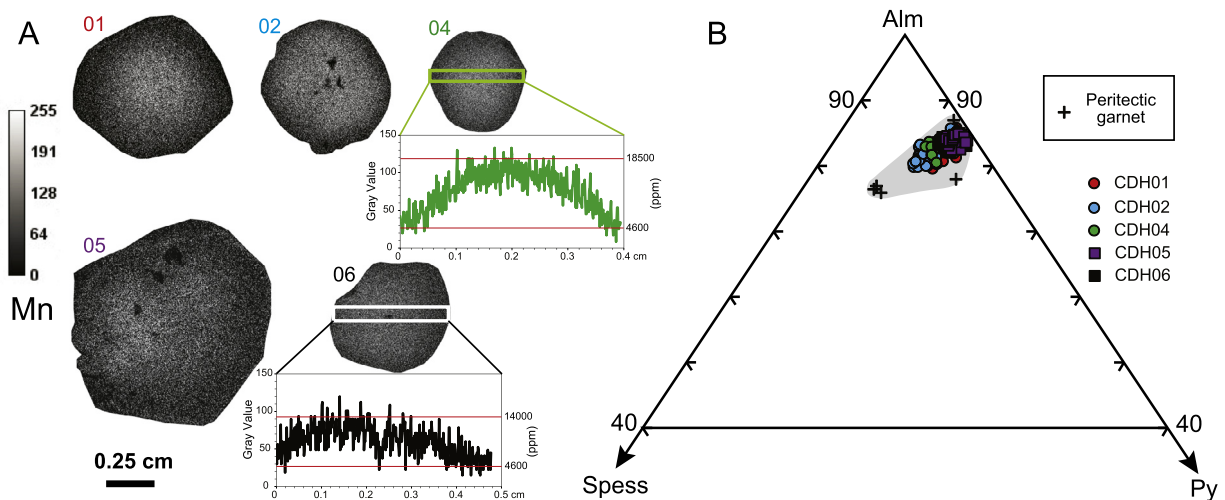
Fig. 2. Micro-XRF map of Mn for five representative garnets (A) and their ternary compositions in mole percent (B). In (A), X-ray intensities are shown along select transects. In (B), previously published compositions of peritectic garnets from Cerro del Hoyazo (Álvarez-Valero et al., 2005, 2007; Cesare et al., 2005) are shown as crosses and compared to our data (colored circles and squares). Cation mole percents for Almandine (Fe^{2+}), Spessartine (Mn^{2+}), and Pyrope (Mg^{2+}) are shown.
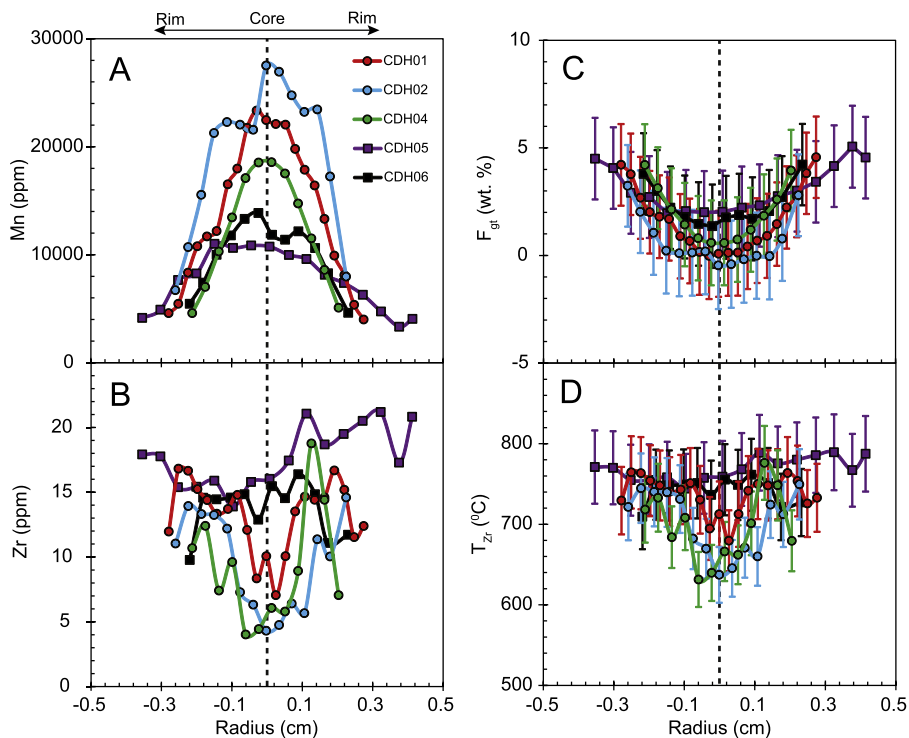

Fig. 3. Zoning profiles for Mn (ppm), Zr (ppm), F_{gt}, and T_{Zr} as a function of radius. F_{gt} is the mass fraction of peritectic garnets formed by breakdown of biotite during partial melting. Calculation is based on modeling of Mn evolution during melting. T_{Zr} is zircon saturation temperature (Celsius) of the melt in equilibrium with the garnet; this is calculated by estimating the Zr content of the melt from the Zr concentration of the garnets and then applying zircon saturation thermometry to the melt. One standard deviation error bars are shown for F_{gt} and T_{Zr}.

4. Discussion

4.1. Garnet zonation records evolution of magma

The elemental zonation patterns described above reflect the composition or conditions of the melt during garnet growth as the rates of crystal growth are much faster than the rates of intra-grain diffusion. For example, 10 Myr are needed for Mn to diffusively homogenize across a 3 mm grain at 800 °C (see Caddick et al., 2010; Carlson, 2006); even longer diffusive timescales are required for REEs and Y. Thus, the strong rim-ward depletion in Mn, Y and HREEs (Figs. 3 and 4) implies that these elements are highly com-

patible in garnet, so that these elements become depleted from the surrounding matrix (partially molten rock) as garnet crystallizes. Successive generations of garnet growth inherit the composition of the matrix, hence the concentration of a compatible element in garnet is inversely related to the integrated amount of garnet formed. The variation in core Mn contents indicates that garnets were nucleating and growing at different times, but the identical Mn contents on the rims, regardless of grain radius and core Mn content, indicates that all garnets were equilibrating with the same matrix up until the time of large-scale segregation of melt. The uniformity of final rim compositions also indicates that the matrix must have been diffusively homogenized. The monotonic decrease
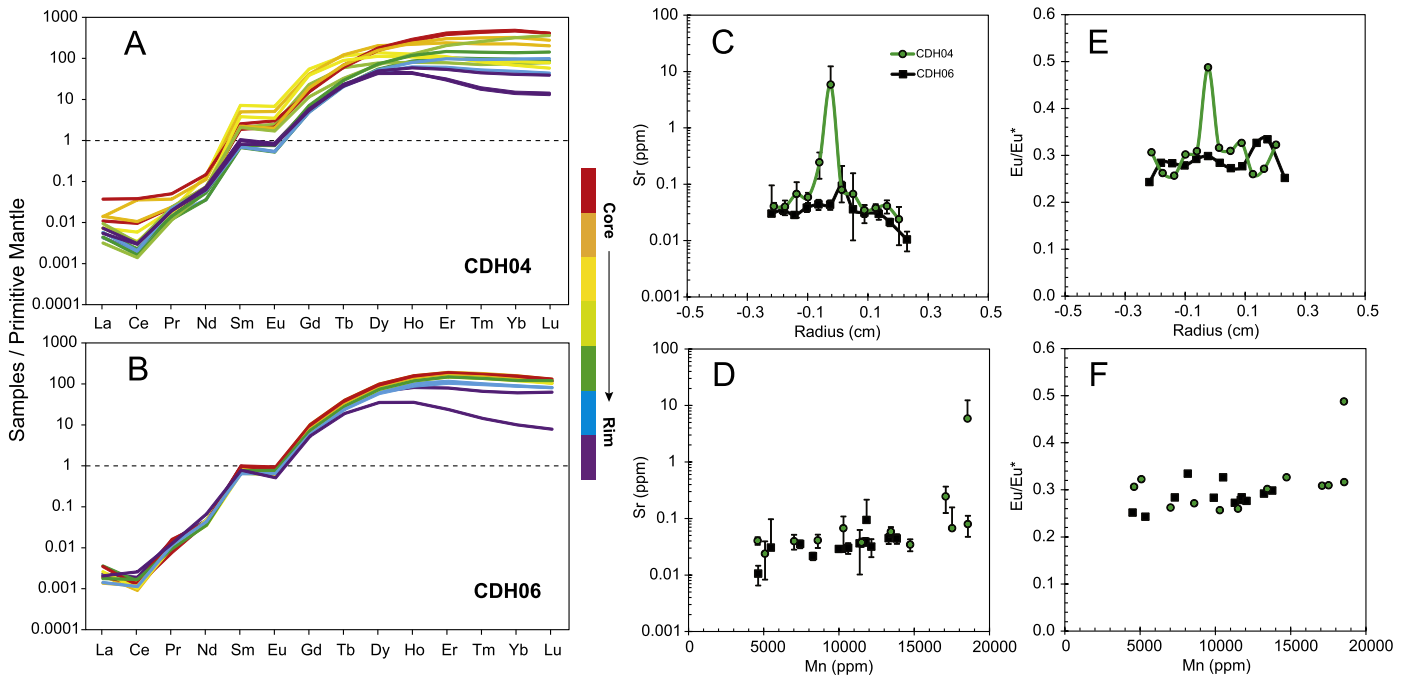
Fig. 4. (A)–(B) Rare earth element patterns for garnets normalized to primitive mantle values (McDonough and Sun, 1995). (C)–(F) Plots of Sr and Eu/Eu* versus garnet radius and Sr and Eu/Eu* versus Mn. Eu/Eu* is equal to $Eu_N/(Sm_N \times Gd_N)^{0.5}$, where subscript N indicates normalization to primitive mantle values. One standard deviation error bars are shown.

in Mn towards the rim indicates that there was never any dissolution of garnet as dissolution/resorption would have led to local enrichment of Mn on the rims.

The rimward increase in Zr followed by a decrease in the outermost rim requires a different explanation (Fig. 3B). We can use the Zr content of the garnet to calculate the Zr content of the melt in equilibrium with the garnet. This requires an estimate of the garnet/melt partition coefficient. Rather than using experimental constraints on garnet Zr partitioning, which are limited and not for bulk system compositions identical to our system, we calculated an empirical partition coefficient using published values of garnet phenocryst and host dacite compositions from the same volcano (Acosta-Vigil et al., 2010; Perini et al., 2009), yielding a garnet/melt partition coefficient of 0.10 ± 0.03 (Table S3). Given the silicic nature of the dacite, we can assume that the system was saturated in zircon. We can then estimate the temperature of the system during garnet growth by using the calculated Zr content of the intergranular melt (determined by dividing the Zr content of the garnet by the empirical partition coefficient) and Zr saturation thermometry (Boehnke et al., 2013; Watson and Harrison, 1983) (Fig. 3), the latter assuming a value of 1.23 ± 0.24 for the compositional factor $M[= (Na + K + 2Ca)/(Al \bullet Si)]$ of plausible melts in our system (Table S4). Our calculations yield temperatures from $631 \pm 34\,°C$ at the core to $789 \pm 47\,°C$ at the rim (see Supplementary Information for methods of error propagation), consistent with increasing temperature during growth of garnet. This increase in calculated zircon-saturation temperature occurs because the Zr content of the melt at zircon saturation increases with temperature. We note that the decrease in Zr on the outermost rim implies a final temperature decrease, but this Zr decrease most likely reflects the point at which zircon is melted out and the system becomes zircon under-saturated, diluting Zr concentrations with further melting. Temperature is thus not reported for the rim.

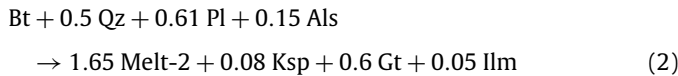### 4.2. Quantifying melt fraction at time of melt segregation

We now attempt to quantify the melt fraction when garnet growth was arrested, representing the time of large-scale melt ex-

traction that led to eruption. Melting of pelites occurs via a series of peritectic reactions. The first involves the breakdown of muscovite (Mu) to form alkali feldspar (Ksp), aluminosilicate (Als) and melt. The early and abrupt decrease in Sr and Eu in the garnet (Fig. 4C–F) indicates complete muscovite breakdown to form alkali feldspar. Feldspar strongly sequesters Sr and Eu and thus, the breakdown of muscovite to feldspar decreases the amount of Sr and Eu available to garnet. We can calculate the total amount of melt (Melt-1) generated from muscovite breakdown using the following stoichiometry constrained experimentally in pelitic systems (Harris et al., 1995; Patiño-Douce and Johnston, 1991),

$$Mu + 0.18\,Pl + 0.18\,Qz \rightarrow 0.3\,Ksp + 0.35\,Als + 0.6\,Melt\text{-}1 \quad (1)$$

where the coefficients are in terms of mass fraction (Mu = muscovite, Pl = plagioclase, Qz = quartz, Ksp = alkali feldspar, Als = aluminosilicate). The muscovite mass fractions of possible pelitic protoliths in the region, such as the Alpujarride metamorphic complex (Massonne, 2014; Ruiz Cruz et al., 2006), are ~30 wt.% (estimate from the modal compositions), so complete muscovite breakdown should have generated ~18 wt.% melt. This stoichiometric constraint on the amount of melt generated per muscovite weight fraction is similar to that inferred from the simplified Na–K–Fe–Mg–Al–Si–H system (Spear et al., 1999).

The second peritectic reaction involves the breakdown of biotite (Bt) with plagioclase (Pl), aluminosilicate (Als) and quartz (Qz) to form alkali feldspar (Ksp), garnet (Gt) and melt. Although muscovite breakdown appears to have been complete, biotite breakdown was not complete because, as discussed above, we see no evidence in the Mn zonation profiles of garnet resorption/consumption as would occur if biotite was exhausted. The fact that the restitic xenoliths in the dacite volcano still contain biotite also indicates incomplete consumption of biotite (e.g., Zeck, 1970; Cesare et al., 1997). The melting stoichiometry (by weight) for biotite (Bt) breakdown (Harris et al., 1995; Patiño-Douce and Johnston, 1991) is given by

$$\text{Bt} + 0.5 \, \text{Qz} + 0.61 \, \text{Pl} + 0.15 \, \text{Als}$$
$$\rightarrow 1.65 \, \text{Melt-2} + 0.08 \, \text{Ksp} + 0.6 \, \text{Gt} + 0.05 \, \text{Ilm} \qquad (2)$$

or

$$\text{Bt} + 0.76 \, \text{Qz} + 0.55 \, \text{Pl} + 0.14 \, \text{Als} \rightarrow 1.72 \, \text{Melt-2} + 0.73 \, \text{Gt} \qquad (3)$$

Because biotite breakdown was not complete, as evidenced by the presence of biotite remaining in the restitic xenoliths, the biotite-derived melt fraction must be estimated indirectly from the amount of peritectic garnet growth. Owing to Mn's high compatibility in garnet, Mn can be used to track the mass fraction of new garnet formed during melting, assuming Rayleigh fractional crystallization of garnet (Fig. 3C),

$$\frac{C_{gt}}{C_{matrix}^0} = D(1 - F_{gt})^{D-1} \qquad (4)$$

where F_{gt} represents the garnet relative to the system, C_{gt} is the concentration of Mn in garnet, C_{matrix}^0 is the concentration of Mn in the matrix (rock + melt), and D is the effective partition coefficient of Mn between the garnet and the matrix. Fractional crystallization is justified because the garnets themselves are not diffusively homogenized but the matrix appears to have been homogeneous as noted above. We assume that the garnet/matrix partition coefficient relevant for our system can be empirically determined from the garnet-bearing dacite. Based on the Mn content of garnet phenocrysts and the host dacite magma (Álvarez-Valero et al., 2007; Cesare et al., 1997), we determine a garnet/dacite magma partition coefficient of 39 ± 6 (Table S5). Mn is so compatible in garnet that the Mn evolution of the system can be modeled by considering garnet as the only significant host of Mn (Mn is compatible in Fe–Ti oxides, but their abundances are not high enough to strongly influence the system's Mn when garnet is present). We take the Mn content of the initial protolith (Ruiz Cruz et al., 2005; Ruiz Cruz, 2010; Ruiz Cruz and Sanz de Galdeano, 2013) to reflect the average composition of meta-pelites in the area (600 ± 441 ppm, Table S6), which has been demonstrated by elemental mass balance to be the source of the dacites (Cesare et al., 1997). Our calculations indicate that the final proportion of peritectic garnet formed since the onset of melting was 4 ± 2 wt.% (see Supplemental Information for methods of error propagation). Using the melting stoichiometry above, this corresponds to 10 ± 5 wt.% fraction of biotite-derived melt (Melt-2). Combining the muscovite- and biotite-derived melts yields a total melt fraction of ~30 wt.% at the time of melt segregation. Due to a density difference between melts and solids, a density correction is required to convert weight fraction to volume fraction of melt (porosity), but given the uncertainties in our calculations, it seems premature to make a density correction. We note that given the positive volume increase associated with generating melt and the negative volume decrease in the solids during transformation of biotite to garnet, our estimates of melt fraction should correspond to minimum estimates of melt porosity. For the rest of the paper, we assume that porosity at the time of melt extraction is similar to that of the critical melt fraction, which is ~30%.

To place these melt fraction estimates into a broader petrogenetic context, we simulated batch melting of a pelitic protolith using the thermodynamic melting program Rhyolite-MELTS (Gualda et al., 2012). We assumed a pressure of 6 kbar, corresponding to thermobarometric estimates from Cesare et al. (1997). Melting was simulated by isobarically increasing temperature for closed systems with bulk water contents ranging from 1 to 3 wt.%. These bulk water contents were chosen in order to encompass a wide range of possible abundance of hydrous minerals, implicitly assuming fluid-absent melting. From a plot of melt fraction versus temperature (Fig. 5A), we see that the higher the bulk water content, the more productive the melting is at near-solidus conditions. We have superimposed on this plot the melt fractions and temperatures estimated from peritectic garnet compositions. This allows us to use our melt fraction-temperature constraints to infer bulk water contents between 1 to 2 wt.%, but certainly not as high as 3 wt.%. The inferred water contents are consistent with the amount of water corresponding to the observed 30–40 wt.% mica content in possible pelitic protoliths in the region (Clemens and Vielzeuf, 1987).

In Fig. 5B and 5C, we show the isobaric melting relationships for 2 wt.% bulk water. Muscovite breakdown melting proceeds to completion early, followed by protracted biotite breakdown with increasing temperature, consistent with the Mn and Zr zonation profiles in garnet. For the range of temperatures inferred from garnet Zr contents, the thermodynamic models yield melt fractions between 40–55 wt.% for 2 wt.% water in the system and 20–30 wt.% for 1 wt.% water in the system, also consistent with that determined independently from garnet chemistry and experimental constraints on melting stoichiometry.

4.3. Geophysical implications of porosity

Our case study of a garnet-bearing dacitic volcano provided an unusual opportunity to estimate the critical porosity for large-scale melt segregation during crustal melting. We estimated a critical porosity of ~30%. Whether this value is unique to the tectonic setting of Cerro del Hoyazo is unclear, but our approach lays the framework for conducting similar studies of other felsic magmas where peritectic crystals can be found. These observations are consistent with theoretical and experimental constraints on critical porosities of 20 to 50% (Arzi, 1978; Renner et al., 2000; Rosenberg and Handy, 2005; Van der Molen and Paterson, 1979; Wickham, 1987). Constraints on the critical trapped melt fractions in granitic plutons, based on coupled trace and major-element systematics, also suggest critical melt fractions of ~30%, although it is important to note that this critical melt fraction is achieved by the cooling and crystallization of a magma rather than re-melting of the crust (Lee and Morton, 2015).

Our observations suggest the possibility that large amounts of melt may reside in the middle to lower crust beneath the volcanically active part of southern Spain. The origin of such melting is most likely related to recent thinning or removal of the subcontinental lithospheric mantle imparted by westward slab rollback in the western Mediterranean (Platt et al., 2013; Turner et al., 1999; Vissers et al., 1995). This appears to have resulted in juxtaposition of hot asthenospheric mantle against thinned lithospheric mantle, resulting in high surface heat flow and melting of the lower crust (e.g., Platt et al., 2013; Turner et al., 1999). Exactly how melt is distributed in the lower crust is unclear. Are regions of 30% melt porosity localized or do such high degrees of melting pervade much of the crust. For example, do large magma chambers, the size of plutons, exist in the crust as in Fig. 6a? Alternatively are high melt fraction regions confined to a thin lens resting on top of a crystalline mush zone, as appears to be the case in mid-ocean ridge environments (Detrick et al., 1987; Kent et al., 1990; Sinton and Detrick, 1992; Toomey et al., 1990) or heterogeneously distributed as thin sills and dikes, perhaps due to variations in source lithology (Fig. 6b)? Indeed, a number of studies in silicic systems in continental environments suggest that crystal-poor magmas tend to occur in thin marginal boundary layers, possibly due to compaction of the magmatic mush (Bachmann and Bergantz, 2004; Hildreth, 1979; Lee et al., 2015). This thin sills would not be visible seismically.

To shed light on this discrepancy between petrology and seismology, we can examine geophysical properties of the crust. Low
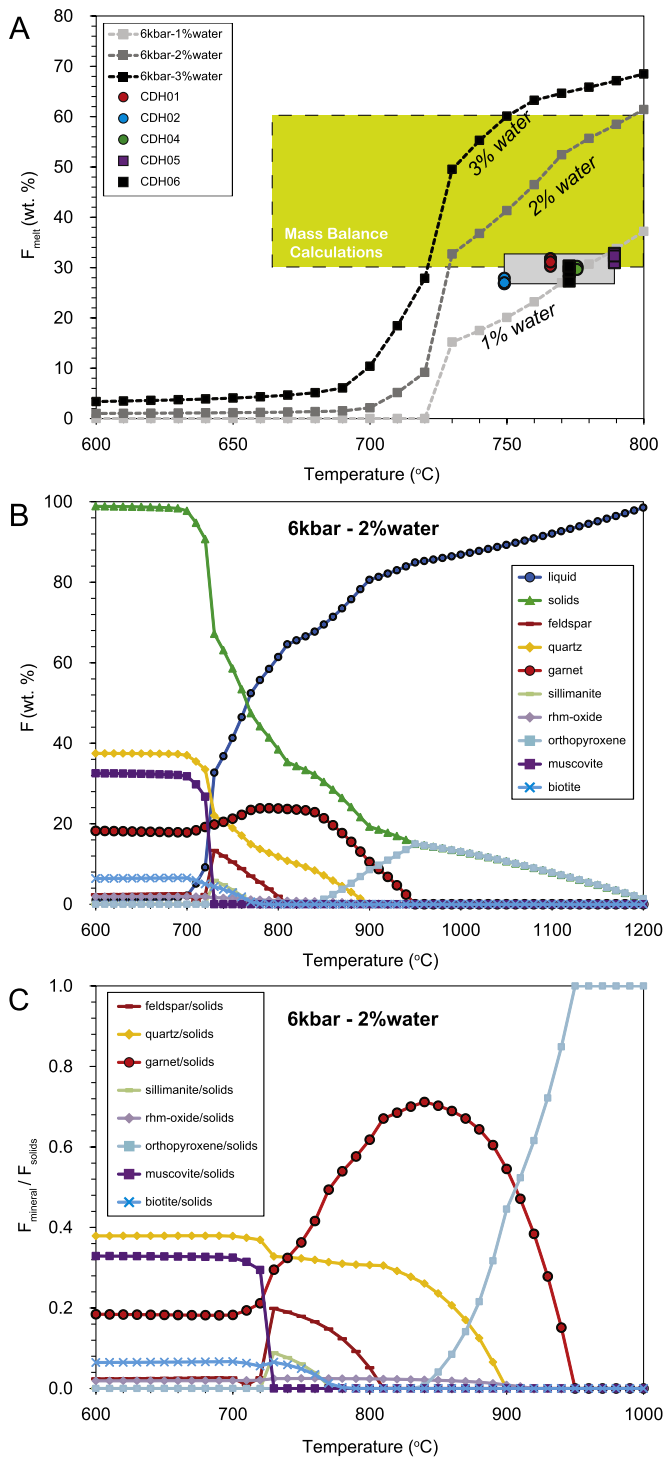
Fig. 6. Cartoon showing two scenarios that can reconcile the greater melt fractions estimated from petrology compared to seismology. (a) Large magma chamber with high melt fractions are ephemeral or highly transient. (b) Presence of high melt porosities in lower continental crust exist in form of thin lenses, sills or dikes.

Fig. 7. Plots of modeled and observed seismic velocity (V_p and V_s) anomalies versus melt porosity for a granitic system (details of calculation in the text). For comparison, reported V_p and V_s anomalies in the middle to lower crust of the Betic orogeny in southern Spain, the Tibetan plateau, and beneath the Yellowstone hotspot in North America are shown for comparison (Carbonell et al., 1998; Farrell et al., 2014; Fu et al., 2010; Thurner et al., 2014; Yuan et al., 2010).

seismic velocities (−6% anomaly in P-wave and −10% anomaly in S-wave) in the middle to lower crust have been reported by active and passive source seismic studies beneath the Betic region (Carbonell et al., 1998; Thurner et al., 2014; Zappone et al., 2000). We can use these velocity anomalies to estimate the average melt porosity of the lower crust by modeling the effects of melt on velocity (Fig. 7A, B). P-wave and S-wave velocities were calculated following the approach of Chu et al. (2010), using the following equations

$$V_p = \sqrt{\frac{K_{eff} + \frac{4}{3}\mu_{eff}}{\rho_{eff}}} \tag{5}$$

$$V_s = \sqrt{\frac{\mu_{eff}}{\rho_{eff}}} \tag{6}$$

where K_{eff} is the effective bulk modulus, μ_{eff} is the effective shear modulus, and ρ_{eff} is the bulk density of the partially molten rock.

Fig. 5. (A) Thermodynamic models of isobaric batch melting of a pelitic protolith based on the rhyolites-MELTS program (Gualda et al., 2012). Mass fraction of melt (F_{melt}) is plotted against temperature T (Celsius) for different bulk system water contents. A pressure of 6 kbars was assumed. F_{melt} and T estimated from garnet chemistry and melting stoichiometry are plotted with the thermodynamic models. Green area represents melt fractions estimated by mass balance between erupted lavas and unmelted protoliths from Cesare et al. (1997) and Acosta-Vigil et al. (2010). Our estimates of F_{melt} correspond to critical melt porosity, whereas melt fractions estimated by mass balance represent aggregate melts, which likely over-estimate critical melt porosity. (B) Thermodynamic models of melting as in (A). Here, phase mass proportions relative to the total mass of the system as a function of temperature are shown for the case of 2 wt.% water in the system. (C) Same as in (B) except mineral modes are reported relative to total solids. Average metapelitic composition is derived from Alpujarride metamorphic complex (Ruiz Cruz et al., 2006). (For interpretation of the references to color in this figure legend, the reader is referred to the web version of this article.)
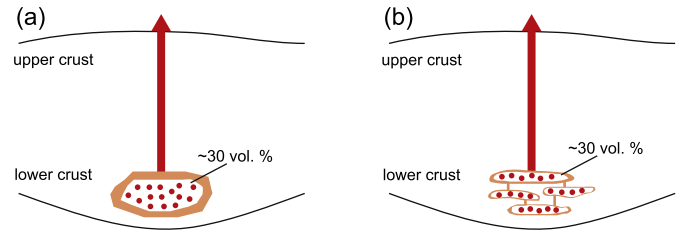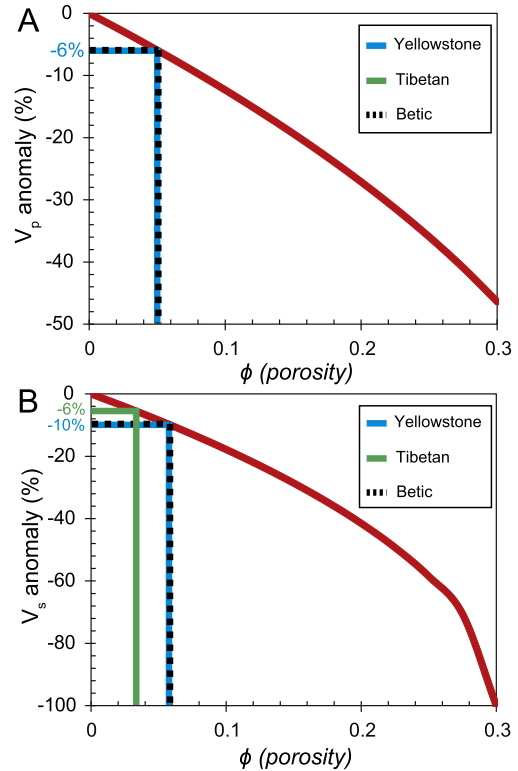
K_{eff} and μ_{eff} are estimated from the elastic properties of the rock and melt following Gassmann (1951),

$$\frac{K_{eff}}{K_0 - K_{eff}} = \frac{K_{dr}}{K_0 - K_{dr}} + \frac{K_m}{\phi(K_0 - K_m)} \tag{7}$$

$$\mu_{eff} = \mu_{dr} \tag{8}$$

where ϕ is porosity, K_0 is the bulk modulus of the material that makes up the framework, K_{dr} is the effective modulus of drained solid matrix, K_m is the bulk modulus of the melt, μ_{dr} is the shear modulus of the drained matrix, and the shear modulus of the melt is assumed to be zero. For porosity below the critical porosity at which the rock transitions from a solid-supported matrix to a melt-supported matrix, K_{dr} and μ_{dr} can be estimated as follows (Nur et al., 1998)

$$K_{dr} = K_0 \left(1 - \frac{\phi}{\phi_c} \right) \tag{9}$$

$$\mu_{dr} = \mu_0 \left(1 - \frac{\phi}{\phi_c} \right) \tag{10}$$

We have adopted K_0 of 55.5 GPa, μ_0 of 34.3 GPa, and K_m of 13.0 GPa for granitic rocks and rhyolitic liquids (Bass, 1995; Levy et al., 2000) at standard state and pressure (STP) conditions. Effective density ρ_{eff} is given by $(1 - \phi)\rho_0 + \phi\rho_m$, where we have assumed $\rho_0 = 2.63$ g/cm^3 and $\rho_m = 2.3$ g/cm^3 at STP conditions (Bass, 1995; Levy et al., 2000). We neglect the effects of temperature and pressure because we are calculating velocity anomalies, that is, the seismic velocities of partially molten rocks relative to unmelted rocks at the same temperature and pressure. We adopt a critical melt porosity of 30% as constrained in this study. Beneath the Betic region, the negative V_p and V_s anomalies of study area correspond to ∼6% of melt (Fig. 7A, B). For comparison, negative V_p and V_s anomalies in the middle and lower crust beneath the Tibetan plateau and the active Yellowstone hotspot (Farrell et al., 2014; Fu et al., 2010; Yuan et al., 2010) indicate ∼3% and ∼6%, beneath the respective regions (Fig. 7A, B).

Seismic constraints on melt porosity appear to be much lower than the 30% melt porosity we estimate in this study at the time of eruption. One explanation for this discrepancy is that the presence of high melt porosities is ephemeral or highly transient (Fig. 6a). Given the high melt productivity associated with peritectic mica breakdown, it is possible that once the system is undergoing heating, melting progresses rapidly to the point of segregation. In such a scenario, the melt porosities of <10%, as determined seismically, may simply reflect background incipient melting. Alternatively, because seismic waves average the velocity structure of the crust over km lengthscales, the large low velocity zones seen in the lower crust beneath magmatically active regions could imply local distribution of high melt porosity zones, such as in the form of thin lenses, sills or dikes (Fig. 6b) (cf. Dufek and Bergantz, 2005). Regardless of how we reconcile the seismic and petrologic constraints on melt porosity, what is clear from our study is that regions of high melt porosity exist, but they are either ephemeral in time or distributed locally and heterogeneously in space. If the latter, the presence of melts could influence the rheology of the lower crust.

5. Conclusion

We show that the critical melt porosity at which large-scale melt segregation occurs during crustal melting can be determined from the zonation of compatible elements in peritectic garnets. As much as 30% interstitial melt can be retained in felsic systems without erupting. Thus, large amounts of melt can be stored in the lower crust of orogenic belts undergoing crustal melting. This may explain why low seismic velocity zones in the lower crust of orogenic belts, inferred to represent regions of extensive melting, are not always expressed at the surface in the form of volcanoes. Storage of significant quantities of melts in the lower crust will have profound implications on the rheology of the lower crust.

Appendix A. Supplementary material

Supplementary material related to this article can be found online at http://dx.doi.org/10.1016/j.epsl.2016.05.025.

References

Acosta-Vigil, A., Cesare, B., London, D., Morgan, G.B., 2007. Microstructures and composition of melt inclusions in a crustal anatectic environment, represented by metapelitic enclaves within El Hoyazo dacites, SE Spain. Chem. Geol. 237, 450–465.

Acosta-Vigil, A., Buick, I., Hermann, J., Cesare, B., Rubatto, D., London, D., Morgan, G.B., 2010. Mechanisms of crustal anatexis: a geochemical study of partially melted metapelitic enclaves and host dacite, SE Spain. J. Petrol. 51, 785–821.

Álvarez-Valero, A.M., Cesare, B., Kriegsman, L.M., 2005. Formation of elliptical garnet in a metapelitic enclave by melt-assisted dissolution and reprecipitation. J. Metamorph. Geol. 23, 65–74.

Álvarez-Valero, A.M., Cesare, B., Kriegsman, L.M., 2007. Formation of spinel–cordierite–feldspar–glass coronas after garnet in metapelitic xenoliths: reaction modelling and geodynamic implications. J. Metamorph. Geol. 25, 305–320.

Arzi, A.A., 1978. Critical phenomena in the rheology of partially melted rocks. Tectonophysics 44, 173–184.

Bachmann, O., Bergantz, G.W., 2004. On the origin of crystal-poor rhyolites: extracted from batholithic crystal mushes. J. Petrol. 45, 1565–1582.

Bass, J.D., 1995. Elasticity of Minerals, Glasses, and Melts. Mineral Physics and Crystallography: A Handbook of Physical Constants, vol. 2, pp. 45–63.

Beaumont, C., Jamieson, R.A., Nguyen, M.H., Lee, B., 2001. Himalayan tectonics explained by extrusion of a low-viscosity crustal channel coupled to focused surface denudation. Nature 414, 738–742.

Berger, A., Kalt, A., 1999. Structures and melt fractions as indicators of rheology in cordierite-bearing migmatites of the Bayerische Wald (Variscan Belt, Germany). J. Petrol. 40, 1699–1719.

Boehnke, P., Watson, E.B., Trail, D., Harrison, T.M., Schmitt, A.K., 2013. Zircon saturation re-revisited. Chem. Geol. 351, 324–334.

Caddick, M.J., Konopásek, J., Thompson, A.B., 2010. Preservation of garnet growth zoning and the duration of prograde metamorphism. J. Petrol. 51, 2327–2347.

Carbonell, R., Sallarés, V., Pous, J., Dañobeitia, J., Queralt, P., Ledo, J., Dueñas, V.G., 1998. A multidisciplinary geophysical study in the Betic chain (southern Iberia Peninsula). Tectonophysics 288, 137–152.

Carlson, W.D., 2006. Rates of Fe, Mg, Mn, and Ca diffusion in garnet. Am. Mineral. 91, 1–11.

Cesare, B., Gomez-Pugnaire, M.T., 2001. Crustal melting in the Alboran domain: constraints from xenoliths of the Neogene volcanic province. Phys. Chem. Earth (A) 26, 255–260.

Cesare, B., Meli, S., Nodari, L., Russo, U., 2005. Fe^{3+} reduction during biotite melting in graphitic metapelites: another origin of CO_2 in granulites. Contrib. Mineral. Petrol. 149, 129–140.

Cesare, B., Salvioli-Mariani, E., Venturelli, G., 1997. Crustal anatexis and melt extraction during deformation in the restitic xenoliths at El Joyazo (SE Spain). Mineral. Mag. 61, 15–27.

Chu, R.S., Helmberger, D.V., Sun, D.Y., Jackson, J.M., Zhu, L.P., 2010. Mushy magma beneath Yellowstone. Geophys. Res. Lett. 37. http://dx.doi.org/10.1029/2009GL041656.

Clemens, J.D., Vielzeuf, D., 1987. Constraints on melting and magma production in the crust. Earth Planet. Sci. Lett. 86, 287–306.

Detrick, R.S., Buhl, P., Vera, E., Mutter, J., Orcutt, J., Madsen, J., Brocher, T., 1987. Multi-channel seismic imaging of a crustal magma chamber along the East Pacific Rise. Nature 326, 35–41.

Dufek, J., Bergantz, G.W., 2005. Lower crustal magma genesis and preservation: a stochastic framework for the evaluation of basalt-crust interaction. J. Petrol. 46, 2167–2195.

Farrell, J., Smith, R.B., Husen, S., Diehl, T., 2014. Tomography from 26 years of seismicity revealing that the spatial extent of the Yellowstone crustal magma reservoir extends well beyond the Yellowstone caldera. Geophys. Res. Lett. 41, 3068–3073.

Fu, Y.V., Li, A., Chen, Y.J., 2010. Crustal and upper mantle structure of southeast Tibet from Rayleigh wave tomography. J. Geophys. Res. 115. http://dx.doi.org/10.1029/2009JB007160.

Gao, S., Liu, X., Yuan, H., Hattendorf, B., Gunther, D., Chen, L., Hu, S., 2002. Determination of forty two major and trace elements in USGS and NIST SRM glasses by laser ablation-inductively coupled plasma-mass spectrometry. Geostand. Newsl. 26, 181–196.

Gassmann, F., 1951. Über die Elastizität poröser Medien. Vierteljahrsschr. Nat.forsch. Ges. Zür. 96, 1–23.

Gualda, G.A., Ghiorso, M.S., Lemons, R.V., Carley, T.L., 2012. Rhyolite-MELTS: a modified calibration of MELTS optimized for silica-rich, fluid-bearing magmatic systems. J. Petrol. 53, 875–890.

Harris, N., Ayres, M., Massey, J., 1995. Geochemistry of granitic melts produced during the incongruent melting of muscovite: implications for the extraction of Himalayan leucogranite magmas. J. Geophys. Res. 100, 15767–15777.

Hildreth, W., 1979. The Bishop Tuff: evidence for the origin of compositional zonation in silicic magma chambers. Spec. Pap., Geol. Soc. Am. 180, 43–76.

Hodges, K.V., 2006. A synthesis of the Channel flow-extrusion hypothesis as developed for the Himalayan–Tibetan orogenic system. Geol. Soc. (Lond.) Spec. Publ. 268, 71–90.

Jiang, H., Lee, C.-T.A., Morgan, J.K., Ross, C.H., 2015. Geochemistry and thermodynamics of an earthquake: a case study of pseudotachylites within mylonitic granitoid. Earth Planet. Sci. Lett. 430, 235–248.

Kent, G.M., Harding, A.J., Orcutt, J.A., 1990. Evidence for a smaller magma chamber beneath the East Pacific Rise at 9 30′N. Nature 344, 650–653.

Le Breton, N., Thompson, A.B., 1988. Fluid-absent (dehydration) melting of biotite in metapelites in the early stages of crustal anatexis. Contrib. Mineral. Petrol. 99, 226–237.

Lee, C.-T.A., Morton, D.M., 2015. High silica granites: terminal porosity and crystal settling in shallow magma chambers. Earth Planet. Sci. Lett. 409, 23–31.

Lee, C.-T.A., Morton, D.M., Farner, M.J., Moitra, P., 2015. Field and model constraints on silicic melt segregation by compaction/hindered settling: the role of water and its effect on latent heat release. Am. Mineral. 100, 1762–1777.

Levy, M., Bass, H., Stern, R., 2000. Handbook of Elastic Properties of Solids, Liquids, and Gases, Four-Volume Set. Academic Press.

Massonne, H.-J., 2014. Wealth of P–T–t information in medium-high grade metapelites: example from the Jubrique Unit of the Betic Cordillera, S Spain. Lithos 208, 137–157.

McDonough, W.F., Sun, S.-S., 1995. The composition of the Earth. Chem. Geol. 120, 223–253.

McKenzie, D., 1984. The generation and compaction of partially molten rock. J. Petrol. 25, 713–765.

Nur, A., Mavko, G., Dvorkin, J., Galmudi, D., 1998. Critical porosity: a key to relating physical properties to porosity in rocks. Lead. Edge 17, 357–362.

Patiño-Douce, A.E., Johnston, A.D., 1991. Phase equilibria and melt productivity in the pelitic system: implications for the origin of peraluminous granitoids and aluminous granulites. Contrib. Mineral. Petrol. 107, 202–218.

Perini, G., Cesare, B., Gömez-Pugnaire, M.T., Ghezzi, L., Tommasini, S., 2009. Armouring effect on Sr–Nd isotopes during disequilibrium crustal melting: the case study of frozen migmatites from El Hoyazo and Mazarron, SE Spain. Eur. J. Mineral. 21, 117–131.

Platt, J.P., Behr, W.M., Johanesen, K., Williams, J.R., 2013. The Betic–Rif arc and its orogenic hinterland: a review. Annu. Rev. Earth Planet. Sci. 41, 313–357.

Renner, J., Evans, B., Hirth, G., 2000. On the rheologically critical melt fraction. Earth Planet. Sci. Lett. 181, 585–594.

Rosenberg, C.L., Handy, M.R., 2005. Experimental deformation of partially melted granite revisited: implications for the continental crust. J. Metamorph. Geol. 23, 19–28.

Ruiz Cruz, M.D., Sanz De Galdeano, C., Lázaro, C., 2005. Metamorphic evolution of Triassic rocks from the transition zone between the Maláguide and Alpujárride complexes (Betic Cordilleras, Spain). Eur. J. Mineral. 17, 81–91.

Ruiz Cruz, M.D., Franco, F., Sanz de Galdeano, C., Novak, J., 2006. Evidence of contrasting low-grade metamorphic conditions from clay mineral assemblages in Triassic Alpujárride–Maláguide transitional units in the Betic Cordilleras, Spain. Clay Miner. 41, 619–636.

Ruiz Cruz, M.D., 2010. Zoned Ca-amphibole as a new marker of the Alpine metamorphic evolution of phyllites from the Jubrique unit, Alpujárride Complex, Betic Cordillera, Spain. Mineral. Mag. 74, 773–796.

Ruiz Cruz, M.D., Sanz De Galdeano, C., 2013. Petrology of microdiamond-bearing schists from the Torrox unit, Betic Cordillera, Spain. Eur. J. Mineral. 25, 919–933.

Rushmer, T., 1995. An experimental deformation study of partially molten amphibolite: application to low-melt fraction segregation. J. Geophys. Res. 100, 15681–15695.

Rushmer, T., 2001. Volume change during partial melting reactions: implications for melt extraction, melt geochemistry and crustal rheology. Tectonophysics 342, 389–405.

Rutter, E.H., Neumann, D.H.K., 1995. Experimental deformation of partially molten Westerly granite under fluid-absent conditions, with implications for the extraction of granitic magmas. J. Geophys. Res. 100, 15697–15715.

Sawyer, E.W., 1996. Melt segregation and magma flow in migmatites: implications for the generation of granite magmas. Trans. R. Soc. Edinb. Earth Sci. 87, 85–94.

Sims, K.W.W., Depaolo, D.J., Murrell, M.T., Baldridge, W.S., Goldstein, S., Clague, D., Jull, M., 1999. Porosity of the melting zone and variations in the solid mantle upwelling rate beneath Hawaii: inferences from ^{238}U–^{230}Th–^{226}Ra and ^{235}U–^{231}Pa disequilibria. Geochim. Cosmochim. Acta 63, 4119–4138.

Sinton, J.M., Detrick, R.S., 1992. Mid-ocean ridge magma chambers. J. Geophys. Res. 97, 216.

Spear, F.S., Kohn, M.J., Cheney, J.T., 1999. P–T paths from anatectic pelites. Contrib. Mineral. Petrol. 134, 17–32.

Thurner, S., Palomeras, I., Levander, A., Carbonell, R., Lee, C.T., 2014. Ongoing lithospheric removal in the western Mediterranean: evidence from Ps receiver functions and thermobarometry of Neogene basalts (PICASSO project). Geochem. Geophys. Geosyst. 15, 1113–1127. http://dx.doi.org/10.1002/2013GC005124.

Toomey, D.R., Purdy, G.M., Solomon, S.C., Wilcock, W.S.D., 1990. The three-dimensional seismic velocity structure of the East Pacific Rise near latitude 9 30′N. Nature 347, 639–645.

Turner, S.P., Platt, J.P., George, R.M.M., Kelley, S.P., Pearson, D.G., Nowell, G.M., 1999. Magmatism associated with orogenic collapse of the Betic-Alboran domain, SE Spain. J. Petrol. 40, 1011–1036.

Van der Molen, I., Paterson, M.S., 1979. Experimental deformation of partially-melted granite. Contrib. Mineral. Petrol. 70, 299–318.

Vielzeuf, D., Holloway, J.R., 1988. Experimental determination of the fluid-absent melting relations in the pelitic system. Contrib. Mineral. Petrol. 98, 257–276.

Vissers, R.L.M., Platt, J.P., Wal, D.v.d., 1995. Late orogenic extension of the Betic Cordillera and the Alboran Domain: a lithospheric view. Tectonics 14, 786–803.

Watson, E.B., Harrison, T.M., 1983. Zircon saturation revisited: temperature and composition effects in a variety of crustal magma types. Earth Planet. Sci. Lett. 64, 295–304.

Wickham, S.M., 1987. The segregation and emplacement of granitic magmas. J. Geol. Soc. 144, 281–297.

Yuan, H., Dueker, K., Stachnik, J., 2010. Crustal structure and thickness along the Yellowstone hot spot track: evidence for lower crustal outflow from beneath the eastern Snake River Plain. Geochem. Geophys. Geosyst. 11. http://dx.doi.org/10.1029/2009GC002787.

Zappone, A., Fernandez, M., Garcıa-Duenas, V., Burlini, L., 2000. Laboratory measurements of seismic P-wave velocities on rocks from the Betic chain (southern Iberian Peninsula). Tectonophysics 317, 259–272.

Zeck, H.P., 1970. An erupted migmatite from Cerro del Hoyazo, SE Spain. Contrib. Mineral. Petrol. 26, 225–246.

Zeck, H.P., Williams, I.S., 2002. Inherited and magmatic zircon from Neogene Hoyazo cordierite dacite, SE Spain – Anatectic source rock Provenance and magmatic evolution. J. Petrol. 43, 1089–1104.